



HAL
open science

3D characterization and modeling of low cycle fatigue damage mechanisms at high temperature in a cast aluminum alloy

Sébastien Dézécot, Vincent Maurel, Jean-Yves Buffière, Fabien Szmytka,
Alain Köster

► **To cite this version:**

Sébastien Dézécot, Vincent Maurel, Jean-Yves Buffière, Fabien Szmytka, Alain Köster. 3D characterization and modeling of low cycle fatigue damage mechanisms at high temperature in a cast aluminum alloy. *Acta Materialia*, 2017, 123, pp.24-34. 10.1016/j.actamat.2016.10.028 . hal-03971030

HAL Id: hal-03971030

<https://hal.science/hal-03971030>

Submitted on 3 Feb 2023

HAL is a multi-disciplinary open access archive for the deposit and dissemination of scientific research documents, whether they are published or not. The documents may come from teaching and research institutions in France or abroad, or from public or private research centers.

L'archive ouverte pluridisciplinaire **HAL**, est destinée au dépôt et à la diffusion de documents scientifiques de niveau recherche, publiés ou non, émanant des établissements d'enseignement et de recherche français ou étrangers, des laboratoires publics ou privés.



Distributed under a Creative Commons Attribution - NonCommercial 4.0 International License

3D characterization and modeling of low cycle fatigue damage mechanisms at high temperature in a cast aluminum alloy

Sebastien Dezecot^{a,b,c,*}, Vincent Maurel^b, Jean-Yves Buffiere^a, Fabien Szmytka^{c,d}, Alain Koster^b

^aINSA-Lyon, MATEIS, UMR CNRS 5510, 69621 Villeurbanne, France

^bMINES ParisTech, Centre des matériaux, UMR CNRS 7633, BP87 91003 Evry, France

^cGroupe PSA, Direction de la Recherche et de l'Innovation Automobile, Route de Gisy, 78943 Vélizy-Villacoublay, France

^dENSTA ParisTech, Unité de Mécanique, Chemin de la Hunière, 91761 Palaiseau Cedex, France

Abstract

Synchrotron X-ray tomography was used to monitor damage evolution in three dimensions during *in situ* Low Cycle Fatigue (LCF) tests at high temperature (250°C) for an industrial material. The studied material is an AlSi7Cu3Mg aluminum alloy (close to ASTM A319) produced by Lost Foam Casting (LFC), a process which generates coarse microstructures but is nevertheless used for engine parts by the automotive industry. The volume analysis (3D images) has shown that cracks are extremely sensitive to microstructural features: coarse pores and hard particles of the eutectic regions are critical regarding respectively the main crack initiation and the crack growth. Finite Elements (FE) simulations, performed on meshes directly generated from 3D volumes and containing only pores, have revealed that mechanical fields also play a major role on the crack behavior. Initiation sites corresponded to areas of maximum inelastic strain while the crack path was globally correlated to high stress triaxiality and inelastic strain fields.

Keywords: X-ray Tomography, Low Cycle Fatigue, A319 Cast Aluminum Alloy, Finite Element, Temperature

1. Introduction

Years ago, car manufacturers chose to reduce the cylinder capacity without decreasing engine power to respond to new environmental regulations [1]. This downsizing aimed at optimizing the power/cylinder capacity in order to reduce polluting emissions. Since then, engine parts, such as cylinder heads and engine blocks, have been experiencing higher operating temperatures induced by the increase of the engine specific power and the combustion flow intensity. This strategy leads to severe loading conditions during start-stop operations or equivalent cyclic loading and contribute to make cylinder heads very critical parts for Thermal-Mechanical Fatigue (TMF) loading[2, 3].

For almost twenty years, most of automotive cylinder heads (gasoline and diesel engines) have been made of aluminum alloys. The most commonly used are hypo-eutectic ones such as ASTM A319 (AlSiCuMg) and A356 (AlSiMg) [4]. Once the material is chosen, the geometry optimization of molded parts is the second most efficient way for reducing the engine mass. The Lost Foam Casting process (LFC), recently introduced in the automotive industry, is well suited for such an optimization [3, 5].

One of the main drawback of cast aluminum alloys is the presence of pores inside the material. These pores have usually a gaseous origin due to the presence of hydrogen [6] or are simple shrinkage cavities; the LFC process tends to increase the population of this second category as large pores are formed during the sublimation of the polystyrene pattern when the mold is filled by the molten metal [7, 8] and by its inherent slow solidification rate. This kind of defect has also a drastic influence on the fatigue behavior

*Corresponding author

Email address: sebastien.dezecot@insa-lyon.fr (Sebastien Dezecot)

of LFC aluminum alloys as cracks frequently initiate at large pores [9, 10, 11, 12]. During High Cycle Fatigue (HCF) tests on cast aluminum alloys, crack initiation almost always occur on surface (or subsurface) pores by slip of dislocations [13] leading to the formation of short mode I cracks on a favorably oriented crystallographic plane [14]. Numerous researchers have also pointed out the influence of hard particles, especially silicon particles, on the mechanical properties of cast aluminum alloy. Tian et al. observe defects (pores, inclusions, oxide films) on nucleation areas in a T6- and a T7-A319 alloys [15]. Furthermore, Huter et al. explain that for high level of plasticity, many crack nucleations first take place in the eutectic regions on pores and/or hard phases for a large range of cast aluminum alloys [16] while initiation occur on the Al/Si interfaces for pure Al-Si alloys [17]. In pore-free materials or when eutectic particles are larger than pores, crack initiation occurs on damaged hard phases [12].

Out-of-phase TMF tests, performed between 100°C and 250°C (with and without dwell time), and Low Cycle Fatigue (LCF) tests have also shown a strong link between microstructure and damage: cracks leading to failure are observed to initiate on pores and to propagate through intermetallic phases at 250°C for an A319 aluminum alloy [3]. However, 2D observations are not sufficient to understand the failure mechanisms as these alloys present a very complex microstructure: fracture surfaces reveal numerous broken particles [3] and the cracking scenario is hard to infer from such observations.

In the last ten years, new methods for the characterization of materials in 3D have emerged [18]. Among those techniques, X-ray Computed Tomography (CT) has the advantage of being non destructive and allows *in situ* observations [18]. Synchrotron radiation, which allows to combine attenuation contrast and phase contrast [19], enhances the capability of the technique for imaging fatigue cracks as well as silicon particles in cast aluminum alloys [20]. If *in situ* fatigue tests have been carried out to follow the initiation and propagation of 3D cracks at room temperature by CT [21, 22], it is only very recently that such *in situ* fatigue tests have also been carried out at high temperature [23, 24]. Besides providing some quantitative information on damage development inside the specimen in relation with the local microstructure, 3D tomographic volumes can also be turned into microstructurally realistic meshes which are used to perform Finite Element (FE) calculations in different fields of materials science, see for instance Withers and Maire for a review on that topic[25].

In this paper, we first describe the damage evolution observed *in situ* in the bulk of a LFC AlSi7Cu3Mg alloy using X ray synchrotron tomography at a temperature relevant for service conditions (250°C) during Low Cycle Fatigue (LCF) testing. Crack initiation and growth mechanisms have been identified. In a second part, FE simulations of the local elasto-viscoplastic (EVP) behavior of the samples are carried out. For this step, a constitutive model inspired by Chaboche work [26] has been used. In spite of the very complex 3D microstructure within the samples, the simulations can successfully predict the *locii* of crack initiation with a simple estimator based on the local inelastic strain.

2. Materials and methods

2.1. Experimental procedures

2.1.1. Material

The material used for this study is a cast AlSi7Cu3Mg aluminum alloy that is widely used for the production of engine parts because of its (relatively) good mechanical properties (and corrosion resistance) at high temperatures and its high quality/cost ratio. Its chemical composition is close to the standard chemistry of the ASTM A319 alloy (Table 1). Cylinder heads were produced by a LFC process and were overaged 500 hours at 250°C to obtain a stabilized metallurgical state [27]. Various cooling rates are naturally obtained in the different parts of a cylinder head leading to large microstructural variations. To obtain samples with a microstructure representative of an inter-valve bridge (critical zone for TMF [2]), samples were directly extracted from cylinder heads by Electro Discharge Machining (EDM). Compared to standard cast Al alloys used in automotive engines, the material studied here is overaged *without* previous solutionizing and has a coarse microstructure as can be seen on figure 1: needle shape Si particles are present as well as Al₂Cu which are not partially dissolved [28, 29].

Si	Fe	Cu	Mn	Mg	Ni	Zn	Ti	Cr
7.30	0.10	3.45	< 0.004	0.31	0.048	< 0.02	0.10	< 0.012

Table 1: Chemical composition (at wt %) of the studied Al alloy obtained by spark optical emission spectrometry on 120 grams of material.

Samples used for this experiment are dumbbell-shaped (see figure 2a). All specimens were mechanically polished (SiC paper down to grit 1000 followed by polishing in a $1\mu\text{m}$ diamond solution) in order to avoid crack initiation on surface scratches and to remove the layer of about $200\mu\text{m}$ which is affected by EDM [30]. After polishing, the mid cross section measures $2.1 \times 2.1\text{mm}^2$.

2.1.2. *In situ* fatigue setup

Isothermal uniaxial *in situ* cyclic damage tests were performed at ID19 beamline at the European Synchrotron Facility (ESRF) in France. The experimental setup is similar to that described by Dezecot et al. [24] and only briefly summarized here. The specimens were cyclically loaded in a small fatigue machine which rotates at the center of a fixed furnace during recording of the tomographic scans. A cyclic load with a stress ratio $R_\sigma=0.1$ and a maximal value of 350 N was applied (imposed displacement of the lower grip) at a frequency of 0.1 Hz at 250°C . Above 150°C , the studied material shows an elastic-viscoplastic behavior which induces stress relaxation during the scans. In order to reduce as much as possible viscoplasticity-induced displacements, fast scans (45 s duration) under maximum load are performed after a dwell time sufficiently long to reach macroscopic stress stabilization (~ 5 min).

2.1.3. Images acquisition and reconstruction

Images were obtained in pink beam mode [31] with a quasi monochromatic beam at an energy of 35 KeV on a CMOS PCO Dimax detector (2016 pixels^2) with a $2.75\mu\text{m}$ pixel size. Attenuation contrast enables to detect copper and iron-rich secondary particles. In addition, the large spatial coherence of the ID19 beam allows to easily distinguish the eutectic silicon particles from the surrounding Al matrix thanks to phase contrast (specimen detector distance 200 mm) [20]. Short cracks a few micrometers long are also easily detected [18]. Volumes, with a $2.75\mu\text{m}$ voxel size, were reconstructed using a Paganin algorithm [32] that enhances contrast between the voids and the aluminum matrix.

2.2. Numerical methods

2.2.1. Mesh generation

The main stages of the meshing process from the 3D tomographic images are as follows:

1. Grey level thresholding of the images to obtain a binary 3D image (so called Vol. A) of the microstructure with the matrix in white and pores (+ air around the sample) in black.
2. Extraction of the outer region to form the Vol. B that fits closely the entire outer surface of the specimen including surface pores. Pores can then be extracted (Vol. C) by a boolean operation between volumes A and B).
3. Generation of two 3D surface meshes (linear triangles) using Avizo [®] commercial software corresponding to the internal pores surfaces from (Vol. C) and the external shape of the sample (Vol. B).
4. Surfaces merging and volume filling with linear tetrahedrons using the Gmsh software [33].
5. Reduction of the number of elements by 3D remeshing of the mesh generated at step 4. The sizes of the elements which are away from the of sample and the pores surfaces are increased using the *Distance* plugin of Gmsh to limit the number of degrees of freedom.

Although each step of segmentation causes a slight morphological alteration of the surfaces, a good description of the pore morphology is obtained. An example of the produced meshes and the localization of the related volume is shown on figure 2b.

2.2.2. Element size

A minimum element size is required to accurately describe the stress/strain evolution away from the pores. A compromise has to be found between CPU time and computation accuracy. A sensitivity analysis was therefore performed to study the influence of the element size on the accuracy of mechanical results. To obtain a relevant analysis, a local criterion has been preferred to global ones. This was carried out on a subvolume containing a single pore extracted from a sample observed by CT as shown on figure 3a. Tensile test conditions were applied on the subvolume. The element size (smallest length that can reach an element edge) at the outer surface is fixed at 200 μm and vary from 15 to 45 μm at the pore surface. Figure 3b shows the result of the simulation in the median plane (labelled Plane M on figure 3a) for a minimum mesh size of 25 μm .

Figure 4 shows the evolution of the σ_{33} stress component for each minimum mesh size tested. The plot corresponds to σ_{33} values extracted at Gauss points from the right border of the pore (point A on figure 3b, $X=936 \mu\text{m}$) along the white arrow shown in figure 3b in direction 1. For the sake of clarity, σ_{33} values are averaged over 2.5 μm intervals. Because the surfacic elements are freely generated by Avizo, a slight offset along the X axis can be observed between different tested meshes. The σ_{33} stress component is the highest near the defect (around 140 MPa) and quickly decreases to 80 MPa. The σ_{33} values are observed to converge at the edge of the pore for tetrahedrons smaller than 30 μm . This value is therefore chosen hereafter.

2.2.3. Behavior law and loading

Specimens are analyzed by CT and representative meshes are generated from the 3D volumes using the meshing protocol of section 2.2.1. FE simulations of the mechanical behavior are performed. Meshes are here composed of a homogeneous aluminum alloy matrix (eutectic phases and intermetallic particles are not modeled) containing pores, as these latter act as preferential crack initiation sites. In this article, only one specimen representative of all studied specimens is described in order to simplify the analysis. The region of interest of the sample is detailed on figure 2b. The simulations were performed using the Zebulon Z-set software [34] with an elasto-viscoplastic Chaboche constitutive model [26]. Model equations are summarized in table 2 while material parameters have been obtained on a stabilized stress/strain loop (see figure 5) of a previously performed LCF test at 250°C [3]. The total strain $\underline{\underline{\varepsilon}}_t$ is decomposed in an elastic $\underline{\underline{\varepsilon}}_e$ (Hooke's law) and an inelastic part $\underline{\underline{\varepsilon}}_{in}$. The yield strength is referenced as R . The evolution of the inelastic strain tensor is defined using a conventional Norton-Hoff flow (K and n parameters) and a non-linear kinematic hardening $\underline{\underline{X}}$ (Armstrong and Frederick's law). $\underline{\underline{s}}$ is the deviatoric part of the stress tensor, $J_2(\underline{\underline{s}} - \underline{\underline{X}})$ defines the second invariant of the tensor $\underline{\underline{s}} - \underline{\underline{X}}$ and \dot{p} is the plastic multiplier. The yield function $f(\underline{\underline{s}} - \underline{\underline{X}}, R) = J_2(\underline{\underline{s}} - \underline{\underline{X}}) - R$ defines the elastic domain according to the von Mises criterion [35].

The simulation aims at reproducing the loading conditions for the synchrotron tests as accurately as possible in terms of temperature (250°C) and applied stresses. The displacement of the bottom surface SB of the meshed volume (see figure 2b) is set to zero while a load is applied on the top surface ST. More details concerning the boundary conditions are available on figure 2b (U1, U2, U3 are respectively displacements in 1, 2, and 3 directions). The load increases linearly during 5 seconds up to the maximal force applied during the experimental test. It then returns to the minimal force in 5 s. This sequence is repeated 50 times without dwell time.

3. Results

3.1. Damage mechanisms, initiation and crack growth

This section describes the damage and its evolution using 2D tomographic slices parallel to a plane containing the stress axis (in XZ plane of figure 2b). For the investigated experimental conditions, crack initiation has consistently been observed to occur in the bulk of the specimen. The different stages leading to the samples rupture from those internal cracks are illustrated on figure 6 where each subfigure corresponds to a specific number of cycles. The tested specimen fails after 50 cycles. Two different and very large pores (labelled P1 and P2) are visible on figure 6. P2 is spherical: probably a gas pore resulting from polymer degassing [8] while P1 is a shrinkage cavity with a much more complex shape.

Strain decomposition	$\underline{\underline{\varepsilon}}_t = \underline{\underline{\varepsilon}}_e + \underline{\underline{\varepsilon}}_{in}$	
Elastic strain	$\underline{\underline{\varepsilon}}_e = \frac{1+\nu}{E} \underline{\underline{\sigma}} - \frac{\nu}{E} tr(\underline{\underline{\sigma}}) \cdot \underline{\underline{I}}$	E=61 GPa ; $\nu=0.33$
Flow rule	$\underline{\underline{\dot{\varepsilon}}}_{in} = \frac{2}{3} \dot{p} \frac{s-X}{J_2(\underline{\underline{s}}-\underline{\underline{X}})}$	
Flow function	$\dot{p} = \frac{2}{3} \left[\frac{J_2(\underline{\underline{s}}-\underline{\underline{X}})-R}{K} \right]^n$	R=33 MPa ; K=120 MPa ; n=6
Kinematic hardening	$\underline{\underline{\dot{X}}} = \frac{2C}{3} \cdot \underline{\underline{\dot{\varepsilon}}}$	C=11150 MPa
	$\underline{\underline{\dot{\alpha}}} = \underline{\underline{\dot{\varepsilon}}}_{in} - \frac{3\dot{p}D}{2C} \underline{\underline{X}}$	D=350

Table 2: Governing equations of the model [26, 35] and parameter identification at 250°C.

The main crack initiation is visible on subfigure 6a that shows the microstructure after two cycles. This initiation results from the rupture of an Al_2Cu particle (marker A) located near a convex part of the large shrinkage pore P1. The crack starts to propagate through silicon particles (marker B on figure 6b) that are present in front of the crack tip. Other ruptures of interdendritic particles occur between cycles 2 and 10 (subfigure 6b) and are visible between the two large pores on figure 6b: Si particles (marker C and E) and Al_2Cu (marker D). With increasing number of cycles, those microcracks merge into a main crack that grows to reach the spherical pore P2 (subfigures 6c and 6d). Hard particles play a crucial part in the propagation process.

Figure 7 shows a projected view of damage orthogonal to the loading direction. This representation reveals the presence of another shrinkage cavity (labeled P3) intersecting the surface in one corner of the specimen; this cavity is not visible on 2D slices presented in figure 6. The subfigures 7b to 7f shows a projected view on the XY plane of the cracks which develop between the two planes represented by thin black lines on figure 7a. For the sake of simplicity, the spherical pore P2 only appear when it is reached by cracks initiated from P1.

A significant crack growth is observed on pore P3 after 20 cycles (see figure 7d). The first propagation stages which occur in the pore vicinity correspond to the merging of the numerous "arms" of pore P3 into a single crack which then moves on toward the sample center after 30 cycles. The crack originating from pore P1 has essentially the same behavior and has joined the spherical pore P2 between 20 and 30 cycles. The growth of this crack leads to the specimen rupture.

Figure 8a and 8b show surface crack growth and associated growth rate curves obtained from the projected views: the crack growth is characterized by the ratio between the measured projected cracked surface S_{proj} and surface of the mid section of the specimen S_{tot} . The crack growth rate during a ΔN interval of cycles is calculated as follows:

$$\frac{1}{S_{tot}} \frac{dS_{proj}}{dN} \simeq \frac{1}{S_{tot}} \frac{\Delta S_{proj}}{\Delta N} \quad (1)$$

Figure 8 reveals that, once initiated, cracks tend to grow quite slowly as the microscopic cracks observed on figure 6b. Figure 8a underlines that crack 1 is larger than crack 2 during all the specimen lifetime. However the surface crack growth rates of figure 8b reveal that the five first cycles have a rather limited impact on global crack growth, crack 2 growing faster than crack 1. Between the 5th and the 20th cycles, crack 2 then slows down while crack 1 accelerates: the ligament between P1 and P2 is then broken. The intersection of crack 1 with pore P2 is marked by an increase of the projected surface between the 20th and the 30th cycles (which is equivalent to the P2 projected surface; see figure 8a). After this event, the crack 1 growth rate becomes close to the global crack growth rate. Crack 1 therefore mainly controls the specimen cracking.

3.2. Mechanical analysis

The 2D pore surface fraction calculated, before testing, on each slice perpendicular to the stress axis and the corresponding stress evolutions along the specimen gage length are shown in figure 9. The presence of a pore leads, as expected, to a local fluctuation of average stress level in the section. The slice/section with the highest stress value ($z \simeq -1800 \mu\text{m}$, see figure 9) corresponds to the location of the first crack. There, the local porosity volume fraction reaches around 4 % (its maximal value).

As cracks initiate close to pores, FE simulations were performed to estimate the effect of the pore morphology on the local strain/stress levels. Figure 10a shows a top view of the specimen mesh as observed along the loading direction. The levels of stress/strain reached in subdomains called SV_i ($i= 1$ to 4) of the mesh at various location in the sample have been calculated. These subdomains integrate all elements intersected by a sphere of a chosen radius, see table 3. SV_1 , 2 and 4 are located in the plane of maximum stress (figure 9) where crack initiation is first observed. Four different locations labeled SV_1 to SV_4 on figure 10 have been selected. The point SV_1 (in red) is located at the center of the Al_2Cu particle labeled A on figure 6 where the first crack appeared. The point SV_2 is placed on the shrinkage surface but on the other side of the defect with respect to SV_1 . The third point, SV_3 , is also placed on the surface of pore P3 (see figure 7) where crack initiation has also occurred. The last point, SV_4 , is placed at the equator of the spherical pore P2 in the closest location to pore P1. The mean local stress/strain curves obtained at these locations within volumes of different sizes (see table 3) are shown on figures 10c to 10h. For comparison purpose, figure 10b shows the stress/strain curve obtained for the whole mesh (ie a significant fraction of the specimen gage volume as visible on figure 2b).

The analysis of the entire studied volume behavior (figure 10b) reveals that, for a prescribed force value of 350 N, the computed stress goes up to 78 MPa and stays almost constant with time (figure 10b). An inelastic strain accumulation during each cycle is observed. This ratchetting is the result of the applied stress amplitude ($R_\sigma > 0$) used during cycling. All other subvolume curves show the same trend of plastic ratchetting but at rates which strongly depend on the location of the volume considered in the mesh as well as on its size.

For example, within the subvolumes centered in SV_1 the maximal stresses and strains range respectively from 88.4 MPa and 0.59 % to 133.7 MPa and 1.51 % when the radius of the volume changes from 100 to 50 μm . Table 4 also shows that although the global stress on the sample remains positive, some compressive stresses can be observed locally due to stress redistribution as a result of a relatively large level of plastic deformation induced by the pore; see for example, the SV_1 -R50 curve on figure 10e: a compressive stress, of the order of -20 MPa is simulated. Although all subdomains analyses are made in the vicinity of pores, the observed mechanical responses appear to be highly dependent on the local morphologies of the defects: stress/strain intensities within SV_1 -R50 are nearly twice as large as those calculated for SV_2 -R50. It is worth pointing out that crack initiation occur on SV_1 -R50 and SV_3 -R50 subdomains, where the stresses and strains are clearly the highest.

Subvolume	Center	Radius	Numbers of elements
SV1-R200	SV1	200 μm	6854
SV1-R100	SV1	100 μm	992
SV1-R50	SV1	50 μm	126
SV2-R50	SV2	50 μm	219
SV3-R50	SV3	50 μm	596
SV4-R50	SV4	50 μm	143

Table 3: Parameters of the subvolumes used for the FE cyclic simulation.

As described above (§ 3.1), crack growth was experimentally observed to interact with different pores, these interactions could be analysed on the basis of FEA. The subfigures 11a and 11b respectively show the plastic strain and the stress triaxiality fields on a vertical slice corresponding approximatively to the plane studied on figure 6. As broken hard particles are experimentally observed after the first mechanical cycles,

Subvolume	Global	SV1-R200	SV1-R100	SV1-R50	SV12-R50	SV3-R50	SV4-R50
σ_{33}^{max} (MPa)	78.7	73.8	88.4	133.7	74.1	118.7	98.6
σ_{33}^{min} (MPa)	3.2	0.6	-5.4	-23.0	-7.0	-9.7	1.61
ε_{cum} (%)	0.51	0.59	0.83	1.51	0.63	1.35	1.07

Table 4: Computed values of σ_{33}^{max} , σ_{33}^{min} and the cumulative plastic strain (evaluated from all cycles) ε_{cum} obtained for the spherical volumes of the mesh listed in table 3 after 50 cycles.

results are extracted from FE computation at the maximum load of the third cycle. These two maps reveal a high strain localization and stress concentration fully consistent with the observed crack path shown by a dashed line on the figure (see also figure 6d). The plastic strain level within the area corresponding to the crack path location is larger than 0.15 % and presents a peak value that reaches more than 0.7 % close to the shrinkage cavity. All elements where the stress triaxiality exceeds 0.5 are also located along the final crack path (and obviously in the shrinkage cavity vicinity) although the maps are extracted only after the third cycle.

Subfigure 11c shows a magnification of the computed plastic strain field close to the shrinkage pore while figure 11d corresponds to the same area extracted from the reconstructed images. The area of maximum local inelastic strain corresponds approximately to the SV1 point on figure 10a and therefore to the first initiation area, where the first broken Al_2Cu phase is observed. Even if other areas inside the entire volume are submitted to high plastic strain levels, the slice represented on the figure 11c shows the most critical area.

4. Discussion

The reconstructed 3D images of the tested sample show clearly that cracks first initiate on hard particles in the vicinity of large pores with complex shapes (shrinkage cavities) in the bulk of the specimen during Low Cycle Fatigue (LCF) tests at 250°C. Figure 6 clearly shows the rupture of an Al_2Cu phase that is located in the vicinity of the largest shrinkage cavity on a plane where the effective stress is the highest. A similar scenario is observed for a second crack (pore P3 in figure 7). A closer examination of the local microstructure reveals that the crack initiates on Si particles located close to the subsurface shrinkage cavity. Crack initiation areas identified for the investigated experimental conditions thus involved two types of defects: pores and hard particles. The presence of a pore seems to be the necessary condition for fatigue crack initiation. This is in agreement with numerous studies which, as mentioned before, show that pores, when present, are the most critical defect which control the fatigue strength of cast aluminum parts. The presence of particles close to shrinkage cavities is inherent to the intrinsic microstructure of cast materials because these particles are formed in eutectic areas (see for example figure 1).

Only one specimen is analyzed here because of the complexity and the general adversity of these simulations. Although FE simulations based on 3D realistic microstructures have become more common [25], as far as we know, it is the first time that computations with so complex loading conditions (temperature, cyclic, large scale yielding, 3D) are exposed. Other specimens have been however studied and modelled; they also show similar damage mechanisms and inelastic strain localizations (see [36] for results at lowest temperatures). In the LFC alloy studied here, the pores size is such that each specimen can be considered as a miniature structure made of a pore-free cast Al alloy. FE simulations based on a homogeneous matrix and pores with a 3D realistic shape were carried out. The FE analysis could in principle be performed at two different length scales: the mesoscopic one where only mean mechanical fields are studied and a more local scale where their local influences on microstructural features are discussed, as exposed later.

The critical plane identified on figure 9 and containing SV1, SV2 and SV4 points is first analyzed. The FE analysis reveals a stress concentration and a strain localization around the pores. The pore nature appears to have an influence on its criticality: higher strain levels are reached around the shrinkage cavity. It seems thus that degassing pores are less harmful to LCF behavior than shrinkage cavities, even if their sizes are equivalent. The local shapes of the pores also play an important role in strain localization. For

the points labeled SV1 and SV2 which are located on the same shrinkage cavity but on opposite sides, the simulated stress/strain curves reveal a larger local stress which result in a larger strain accumulation at SV1 than at SV2 and in a complex stress state (local compressive stresses during global positive stress loading). This observation is in agreement with other FE results using realistic pores generated thanks to X-ray tomography [36]: fatigue cracks tend to initiate on the parts of the pores showing a higher local curvature [37, 38]. The results presented on figure 11 show that the first/main crack initiation site corresponds to locations where the inelastic strain is maximum. This inelastic strain localization is also observed in another plane for the second crack near SV3 point (figure 7). This indicator seems thus to correctly localize critical areas in our case which correspond to severe mechanical loading (LCF). The use of such an indicator based on the inelastic deformation rather than a maximum stress or a stress concentration factor has been suggested by other authors to identify critical areas with respect to fatigue in cast aluminum alloys [39, 40]. An error on the estimation of stress or strain quantities can however predict an incorrect localization of critical area. An energetic approach can reduce these errors and gives more robustness to the analysis. The dissipative energy formulated by Maurel *et al.* was used in this work: $W_p = \int_{cycle} \underline{s} : d\underline{\varepsilon}_{in}$ where \underline{s} and $\underline{\varepsilon}_{in}$

stand respectively for the deviatoric stress and the inelastic strain tensors [41]. Figure 12 shows the average dissipative energies computed along a line corresponding to the intersection of the surface of the shrinkage cavity responsible of the first crack initiation and the critical plane identified by figure 9. All energies were previously calculated on the first three cycles on spherical subvolumes with 50 μm radii and were averaged to estimate an equivalent dissipative energy per cycle. The damaged areas observed experimentally after 5 cycles (white areas on figure 12) correlate very well with the zones where the computed plastic energy W_p are the highest. This approach based on the dissipated inelastic energy seems therefore very promising in order to predict critical areas toward LCF behavior at a mesoscopic scale in an engineering approach [2, 42]. This criterion correctly predicts the location of initiation sites on small specimens and seems interesting for damage simulation on FE models of cylinder heads where pores are included. Pores could be included using X-ray tomographic data with degraded spatial resolution (since only the largest pores play a role on LCF behavior) or using predictions of foundry models [43, 44, 45].

Numerical simulations with simple meshes which only include pores give mechanical information to better understand the mechanisms that lead to the rupture/debonding of particles even if the latter are not explicitly integrated into the simulations. They allow to have a global view of the crack path using simple mechanical quantities by post processing analysis, see for example figure 11a. The crack path (composed of broken particles), visible on figure 6d, corresponds to the areas of plastic strain localization induced by the structural effect due to the large pores. It is conventionally accepted that the strain incompatibility between the hard particles (particularly brittle Si particles [46]) and the aluminum matrix produces cleavage or debonding of hard phases [47, 40]. At high temperature, the matrix mechanical behavior (Young modulus and hardness) decreases and this evolution is more pronounced than for the other components (Si and Al_2Cu particles) [48]. These incompatibilities are therefore more pronounced at high temperature and increase the risk of particles cleavage and debonding.

Areas where large plastic strains are predicted, are also submitted to high stress triaxiality levels as visible on figure 11b. In situation of large scale yielding, the damage evolution seems close to what is observed during monotonic testing on ductile materials where stress triaxiality plays a crucial role. For instance, Goghale *et al.* have shown that higher stress triaxiality leads to an increase in the damage rate of silicon particles during tensile tests for different temperatures between -50 and 125°C [49]. Also, according to Dighe *et al.*, damage within Si particles seems to be coupled with the onset of necking during tensile testing [50]. In our work necking is also observed (see for example figure 6) and could explain why many damaged particles are visible on the tomographic slices. According to Dighe *et al.* a critical amount of hydrostatic stress (equivalent to high triaxiality levels) is required to initiate Si particles debonding. Although particles are not included into the simulation, the "real" localization areas of inelastic strain and stress triaxiality in the material should be globally similar because these two mechanical quantities are known to be locally higher around hard particles. FE simulations on simplified representative cells show for example that silicon particles accumulate plastic strain in their wake [51, 39] and particularly when the particle is located in the vicinity of a pore [39]. Studies on particulate-reinforced metal-matrix composites also show higher stress

triaxiality levels around particles whose sizes are close to the silicon particles in the present material [52, 53].

The overall crack path seems therefore controlled by the mechanical loading which induce damage within the hard particles (via inelastic strain and stress triaxiality). This damage is visible in front of the crack tip incidentally. It is generally a particle that is not in direct contact with the crack (or the pore, before initiation) which is first broken: this is characteristic of a high stress triaxiality level. The maximum stress triaxiality is indeed not located exactly at the crack tip but just in front of it on notched specimens during fracture of ductile materials [54, 55, 56, 57]. This phenomenon can also be observed in figure 4 for the smallest mesh sizes (bellow $35 \mu\text{m}$); the normal stress is maximum at around $15 \mu\text{m}$ of the pore surface for a typical degassing pore.

The sizes of the studied specimens are small in order to be compatible with CT observations; therefore, only the first stages of crack growth can be analyzed. The explicit modelling of crack growth is not proposed in this article because no criterion are currently available in 3D for fatigue crack growth and crack branching under large scale yielding (and high temperatures), even if it is an active research topic [41]. Available models are only available for classical 2D cracking analysis [41, 58]. LCF tests on macroscopic Single Edge Notch Tension specimens are currently being carried out [59] in order to validate crack initiation and crack growth mechanisms on larger volumes representative of inter-valve bridges.

5. Conclusions

Using X-ray synchrotron microtomography and a specific experimental setup, the LCF behavior of an Al-Si-Cu-Mg alloy produced by a LFC process has been studied *in situ* at 250°C . Tomographic volumes helped to understand the role of the complex 3D microstructure of this material: eutectic particles are interconnected and large (up to $\sim 1 \text{ mm}$) shrinkage cavities have a complex morphology. In addition it has been possible to analyze crack initiation and, to some extent, crack growth in the bulk.

A microstructure based FE model representative of the 3D porous microstructure has been generated from tomographic volumes in order to perform EVP cyclic FE simulations. The results of those simulations have shown the major influence of the pore morphology on the mechanical fields. The initiation sites of cracks have been shown to be located in the vicinity of shrinkage cavities where the dissipated inelastic energy during cycling is maximum. Degassing pores with a more spherical shape are less critical at equivalent size. The global crack path corresponds to areas of strain localization. Hard particles (intermetallic and/or Si particles) are extensively damaged ahead of the crack which propagates along those damaged zones. The proposed approach which combines experimental observations and numerical simulations, is essential for understanding the damage mechanisms which operate in this complex microstructure; it provides some invaluable information for the development of damage criteria because quantities such as the level of stress triaxiality or the dissipated inelastic energy are not directly measurable during experiments.

A scenario for damage development during LCF can be suggested (see figure 13):

- High local plastic strain levels develop near large microshrinkage pores with complex shapes.
- Hard particles located in these zones are damaged during the first mechanical cycles (step I on figure 13a).
- The initiation (step II) appears when the matrix ligament between the pore and the damaged particle is broken (see figure 13b).
- During cycling, particles in front of the new crack tip are progressively damaged (step III on figure 13c).
- The propagation consists of a repetition of step I and II mechanisms. The cracks remain confined within the eutectic regions which are located inside the highly stressed areas ahead of the crack tip.

6. Acknowledgements

The authors thank the French National Research Agency for funding this study through the ANR project INDIANA (grant ANR-12-RMNP-0011) and the French National Association for Research and Technology for the partial funding of a PhD student (SD). We also thank Elodie Boller and Jean-Paul Valade from ESRF ID 19 beamline, Pierre Osmond from PSA Group for the material heat treatment supervision and Eric Charkaluk, Nora Dahdah, Ahmed El-Bartali, Nathalie Limodin, and Jean-Francois Witz from Laboratoire de Mécanique de Lille for their assistances during the tests.

References

- [1] T. E. P. a. of the Council, Regulation (EU) No 333/2014 of the European Parliament and of the Council of 11 March 2014 amending Regulation (EC) No 443/2009 to define the modalities for reaching the 2020 target to reduce CO₂ emissions from new passenger cars (Mar. 2014).
URL http://eur-lex.europa.eu/legal-content/EN/TXT/?uri=uriserv:OJ.L_.2014.103.01.0015.01.ENG
- [2] F. Szmytka, A. Oudin, A reliability analysis method in thermomechanical fatigue design, *Int. J. Fatigue* 53 (2013) 82–91.
- [3] S. Tabibian, E. Charkaluk, A. Constantinescu, F. Szmytka, A. Oudin, TMF-LCF life assessment of a Lost Foam Casting A319 aluminum alloy, *Int. J. Fatigue* 53 (2013) 75–81. doi:10.1016/j.ijfatigue.2012.01.012.
- [4] M. Javidani, D. Larouche, Application of cast Al-Si alloys in internal combustion engine components, *Int. Mater. Rev.* 59 (3) (2014) 132–158. doi:10.1179/1743280413Y.0000000027.
- [5] N. Limodin, A. El Bartali, L. Wang, J. Lachambre, J.-Y. Buffiere, E. Charkaluk, Application of X-ray microtomography to study the influence of the casting microstructure upon the tensile behaviour of an Al-Si alloy, *Nucl. Instrum. Meth. B.* 324 (2014) 57–62, wOS:000333791600010. doi:10.1016/j.nimb.2013.07.034.
- [6] R. Lumley, *Fundamentals of aluminium metallurgy: Production, processing and applications*, Elsevier, 2010.
- [7] J. R. Brown, The lost foam casting process, *Met. Mater.* 8 (10) (1992) 550–555.
- [8] S. Shivkumar, L. Wang, D. Apelian, The lost-foam casting of aluminum alloy components, *JOM-J. Min. Met. Mat. S.* 42 (11) (1990) 38–44.
- [9] M. J. Couper, A. E. Neeson, J. R. Griffiths, Casting defects and the fatigue behaviour of an aluminium casting alloy, *Fatigue Fract. Eng. M.* 13 (3) (1990) 213–227.
- [10] Q. G. Wang, D. Apelian, D. A. Lados, Fatigue behavior of A356-T6 aluminum cast alloys. Part I. Effect of casting defects, *J. Light Met.* 1 (1) (2001) 73–84.
- [11] H. R. Ammar, A. M. Samuel, F. H. Samuel, Porosity and the fatigue behavior of hypoeutectic and hypereutectic aluminumsilicon casting alloys, *Int. J. Fatigue* 30 (6) (2008) 1024–1035.
- [12] S. Dezecot, M. Brochu, Microstructural characterization and high cycle fatigue behavior of investment cast A357 aluminum alloy, *Int. J. Fatigue* 77 (2015) 154–159. doi:10.1016/j.ijfatigue.2015.03.004.
- [13] C. Bathias, A. Pineau, *Fatigue of materials and structures*, John Wiley & Sons, 2013.
- [14] M. Brochu, Y. Verreman, F. Ajersch, D. Bouchard, High cycle fatigue strength of permanent mold and rheocast aluminum 357 alloy, *Int. J. Fatigue* 32 (8) (2010) 1233–1242.
- [15] D. Tian, X. Liu, G. He, Y. Shen, S. Lv, Q. Wang, Low cycle fatigue behavior of casting A319 alloy under two different aging conditions, *Mat. Sci. Eng. A - Struc.* 654 (2016) 60–68. doi:10.1016/j.msea.2015.12.023.
- [16] P. Huter, P. Renhart, S. Oberfrank, M. Schwab, F. Grn, B. Stauder, High-and low-cycle fatigue influence of silicon, copper, strontium and iron on hypo-eutectic AlSiCu and AlSiMg cast alloys used in cylinder heads, *Int. J. Fatigue*.
- [17] J. Stolarz, O. Madelaine-Dupuich, T. Magnin, Microstructural factors of low cycle fatigue damage in two phase AlSi alloys, *Mat. Sci. Eng. A - Struc.* 299 (1) (2001) 275–286.
- [18] J.-Y. Buffiere, E. Maire, *Imagerie 3D en mécanique des matériaux, Traité MIM, série Matériaux*, Lavoisier, 2014.
- [19] P. Cloetens, M. Pateyron-Salomé, J. Y. Buffiere, G. Peix, J. Baruchel, F. Peyrin, M. Schlenker, Observation of microstructure and damage in materials by phase sensitive radiography and tomography, *J. Appl. Phys.* 81 (9) (1997) 5878–5886.
- [20] W. Ludwig, J.-Y. Buffiere, S. Savelli, P. Cloetens, Study of the interaction of a short fatigue crack with grain boundaries in a cast Al alloy using X-ray microtomography, *Acta Mater.* 51 (3) (2003) 585–598.
- [21] J.-Y. Buffiere, E. Maire, J. Adrien, J.-P. Masse, E. Boller, In situ experiments with X ray tomography: an attractive tool for experimental mechanics, *Exp. Mech.* 50 (3) (2010) 289–305.
- [22] P. J. Withers, M. Preuss, Fatigue and damage in structural materials studied by X-ray tomography, *Annu. Rev. Mater. Res.* 42 (2012) 81–103.
- [23] T. Chapman, K. Kareh, M. Knop, T. Connolley, P. Lee, M. Azeem, D. Rugg, T. Lindley, D. Dye, Characterisation of short fatigue cracks in titanium alloy IMI 834 using X-ray microtomography, *Acta Mater.* 99 (2015) 49–62. doi:10.1016/j.actamat.2015.07.069.
- [24] S. Dezecot, J.-Y. Buffiere, A. Koster, V. Maurel, F. Szmytka, E. Charkaluk, N. Dahdah, A. El Bartali, N. Limodin, J.-F. Witz, In situ 3d characterization of high temperature fatigue damage mechanisms in a cast aluminum alloy using synchrotron X-ray tomography, *Scripta Mater.* 113 (2016) 254–258. doi:10.1016/j.scriptamat.2015.11.017.
- [25] E. Maire, P. J. Withers, Quantitative X-ray tomography, *Int. Mater. Rev.* 59 (1) (2014) 1–43.
- [26] J. L. Chaboche, A review of some plasticity and viscoplasticity constitutive theories, *Int. J. Plasticity* 24 (10) (2008) 1642–1693.

- [27] S. Tabibian, E. Charkaluk, A. Constantinescu, G. Guillemot, F. Szymtka, Influence of process-induced microstructure on hardness of two AlSi alloys, *Mat. Sci. Eng. A - Struc.* 646 (2015) 190–200. doi:10.1016/j.msea.2015.08.051.
- [28] B. Barlas, Etude du comportement et de l'endommagement en fatigue d'alliages d'aluminium de fonderie, Ph.D. thesis, École Nationale Supérieure des Mines de Paris (2004).
- [29] A. M. Samuel, J. Gauthier, F. H. Samuel, Microstructural aspects of the dissolution and melting of Al₂Cu phase in Al-Si alloys during solution heat treatment, *Metall. Mater. Trans. A* 27 (7) (1996) 1785–1798.
- [30] S. Kumar, R. Singh, T. P. Singh, B. L. Sethi, Surface modification by electrical discharge machining: A review, *J. Mater. Process. Tech.* 209 (8) (2009) 3675–3687. doi:10.1016/j.jmatprotec.2008.09.032.
- [31] P. Willmott, An introduction to synchrotron radiation: Techniques and applications, John Wiley & Sons, 2011.
- [32] D. Paganin, S. C. Mayo, T. E. Gureyev, P. R. Miller, S. W. Wilkins, Simultaneous phase and amplitude extraction from a single defocused image of a homogeneous object, *J. Microsc.* 206 (1) (2002) 33–40.
- [33] C. Geuzaine, J.-F. Remacle, Gmsh: A 3D finite element mesh generator with builtin preand postprocessing facilities, *Int. J. Num. Meth. Eng.* 79 (11) (2009) 1309–1331.
- [34] Z-set webpage.
URL <http://www.zset-software.com>
- [35] J. Lemaitre, J.-L. Chaboche, A. Benallal, R. Desmorat, Mécanique des matériaux solides-3eme édition, Dunod, 2009.
- [36] S. Dezecot, J.-Y. Buffiere, A. Koster, V. Maurel, F. Szymtka, Characterization of damage in a cast aluminum alloy during cyclic loading test at high temperature by x-ray tomography, in: COM 2015-The conference of metallurgists, 2015.
- [37] G. Nicoletto, R. Konen, S. Fintova, Characterization of microshrinkage casting defects of AlSi alloys by X-ray computed tomography and metallography, *Int. J. Fatigue* 41 (2012) 39–46.
- [38] I. Serrano Munoz, Influence of casting defects on the fatigue behaviour of an A357-T6 aerospace alloy, Ph.D. thesis, Institut National des Sciences Appliquées de Lyon (2014).
- [39] Y. Gao, J. Yi, P. Lee, T. Lindley, A micro-cell model of the effect of microstructure and defects on fatigue resistance in cast aluminum alloys, *Acta Mater.* 52 (19) (2004) 5435–5449. doi:10.1016/j.actamat.2004.07.035.
- [40] K. Gall, N. Yang, M. Horstemeyer, D. L. McDowell, J. Fan, The debonding and fracture of Si particles during the fatigue of a cast Al-Si alloy, *Metall. Mater. Trans. A* 30 (12) (1999) 3079–3088.
- [41] V. Maurel, L. Rémy, F. Dahmen, N. Haddar, An engineering model for low cycle fatigue life based on a partition of energy and micro-crack growth, *Int. J. Fatigue* 31 (5) (2009) 952–961.
- [42] S. Fontanesi, M. Giacomini, Multiphase CFD/CHT optimization of the cooling jacket and FEM analysis of the engine head of a V6 diesel engine, *Appl. Therm. Eng.* 52 (2) (2013) 293–303.
- [43] Flow3d: Solidification and shrinkage defects webpage.
URL <http://www.flow3d.com/home/industries/metal-casting/defect-prediction/solidification-defects>
- [44] D. Gunasegaram, D. Farnsworth, T. Nguyen, Identification of critical factors affecting shrinkage porosity in permanent mold casting using numerical simulations based on design of experiments, *J. Mater. Process. Tech.* 209 (3) (2009) 1209–1219. doi:<http://dx.doi.org/10.1016/j.jmatprotec.2008.03.044>.
- [45] O. Koeser, B. Kalkunte, R. Yang, N. Hai, Centrifugal casting of large ti-6al-4v structural components supported by process modelling, in: 71st Worl Foundry Congress, 2014.
- [46] M. Mueller, M. Fornabaio, G. agar, A. Mortensen, Microscopic strength of silicon particles in an aluminiumsilicon alloy, *Acta Mater.* 105 (2016) 165–175. doi:10.1016/j.actamat.2015.12.006.
- [47] J.-Y. Buffiere, S. Savelli, P.-H. Jouneau, E. Maire, R. Fougères, Experimental study of porosity and its relation to fatigue mechanisms of model AlSi7Mg0.3 cast Al alloys, *Mat. Sci. Eng. A - Struc.* 316 (1) (2001) 115–126.
- [48] C.-L. Chen, A. Richter, R. C. Thomson, Investigation of mechanical properties of intermetallic phases in multi-component AlSi alloys using hot-stage nanoindentation, *Intermetallics* 18 (4) (2010) 499–508.
- [49] A. M. Gokhale, M. D. Dighe, M. Horstemeyer, Effect of temperature on silicon particle damage in A356 alloy, *Metall. Mater. Trans. A* 29 (3) (1998) 905–907.
- [50] M. D. Dighe, A. M. Gokhale, M. F. Horstemeyer, Effect of loading condition and stress state on damage evolution of silicon particles in an Al-Si-Mg-base cast alloy, *Metall. Mater. Trans. A* 33 (3) (2002) 555–565.
- [51] J. Fan, D. L. McDowell, M. F. Horstemeyer, K. Gall, Cyclic plasticity at pores and inclusions in cast AlSi alloys, *Eng. Fract. Mech.* 70 (10) (2003) 1281–1302.
- [52] G. Meijer, F. Ellyin, Z. Xia, Aspects of residual thermal stress/strain in particle reinforced metal matrix composites, *Compos. Part B: Eng.* 31 (1) (2000) 29–37.
- [53] Z. Wang, T.-K. Chen, D. J. Lloyd, Stress distribution in particulate-reinforced metal-matrix composites subjected to external load, *Metall. Trans. A* 24 (1) (1993) 197–207.
- [54] C. R. Chen, O. Kolednik, J. Heerens, F. D. Fischer, Three-dimensional modeling of ductile crack growth: Cohesive zone parameters and crack tip triaxiality, *Eng. Fract. Mech.* 72 (13) (2005) 2072–2094.
- [55] F. Rivalin, J. Besson, A. Pineau, M. Di Fant, Ductile tearing of pipeline-steel wide plates: II. Modeling of in-plane crack propagation, *Eng. Fract. Mech.* 68 (3) (2001) 347–364.
- [56] A. Pineau, A. A. Benzerga, T. Pardoen, Failure of metals I: Brittle and ductile fracture, *Acta Mater.* 107 (2016) 424–483.
- [57] D. Broek, Elementary engineering fracture mechanics, Springer Science & Business Media, 2012.
- [58] B. Tomkins, Fatigue crack propagation analysis, *Philos. Mag.* 18 (155) (1968) 1041–1066.
- [59] S. Dezecot, Caractérisation et modélisation du rôle des défauts microstructuraux dans la fatigue oligocyclique des alliages d'aluminium de fonderie : application au procédé à modèle perdu, Ph.D. thesis, Institut National des Sciences Appliquées de Lyon (In progress).

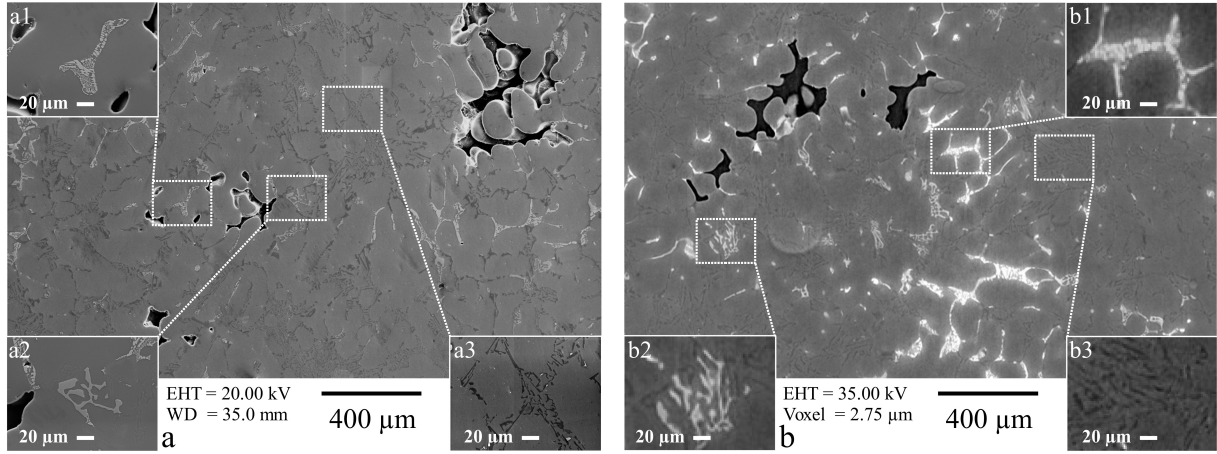


Figure 1: Comparison of the studied alloy microstructure as observed by (a) SEM and (b) synchrotron X-ray tomography. The corner pictures show magnifications of the main eutectic particles : a1 and b1 for θ -Al₂Cu phases, a2 and b2 for α -AlFeSi intermetallics and, a3 and b3 for silicon particles.

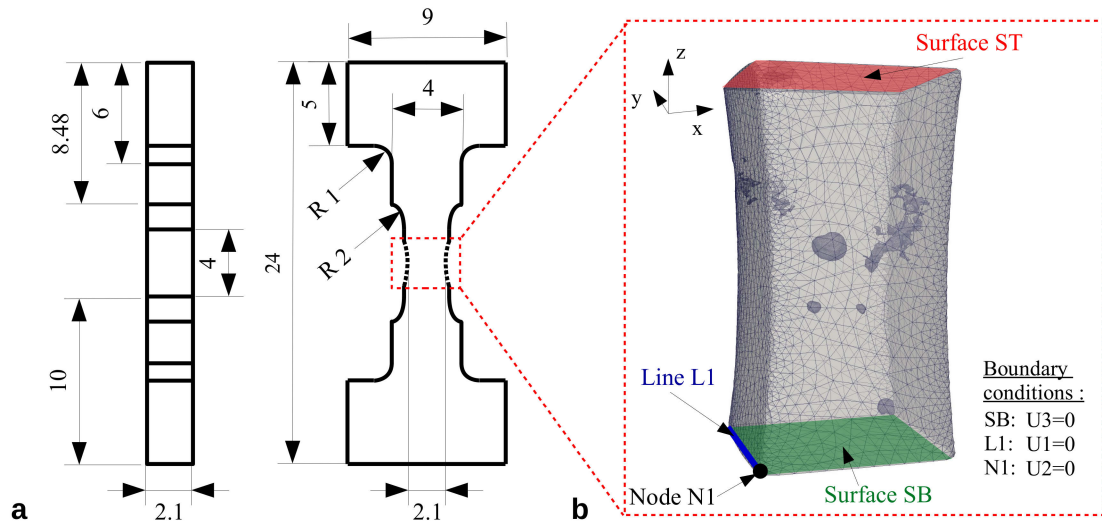


Figure 2: (a) Fatigue specimen geometry (dimensions are in millimeters). The geometry of the central area is slightly curved due to a final manual polishing. (b) 3D rendering of the mesh generated from studied volume and boundary conditions. The loading is applied on surface ST while displacement orthogonal to surface SB is set to zero.

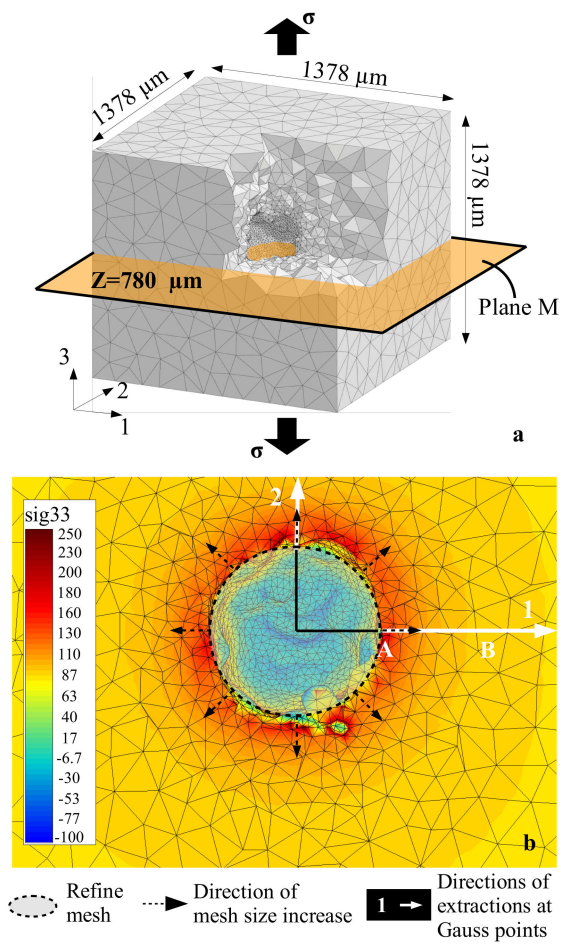


Figure 3: (a) Subvolume used for the mesh sensitivity analysis and (b) stress component σ_{33} evaluated on the $Z=780 \mu\text{m}$ plane orthogonal to the loading direction.

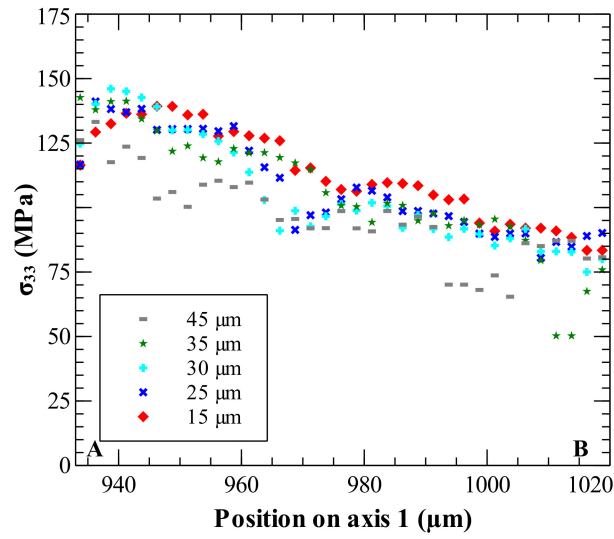


Figure 4: Evolution of the stress component σ_{33} on the pore vicinity along direction 1 shown on figure 3b for different element sizes.

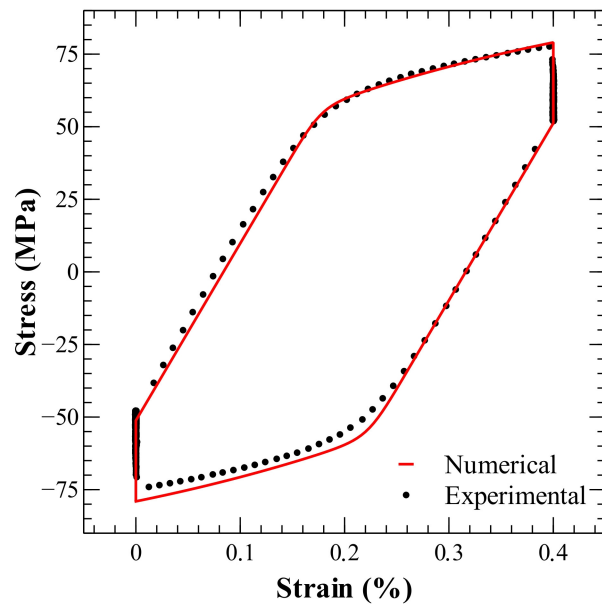


Figure 5: Experimental and numerical stress/strain loops of the studied material at 250°C. The experimental curve is obtained from [3].

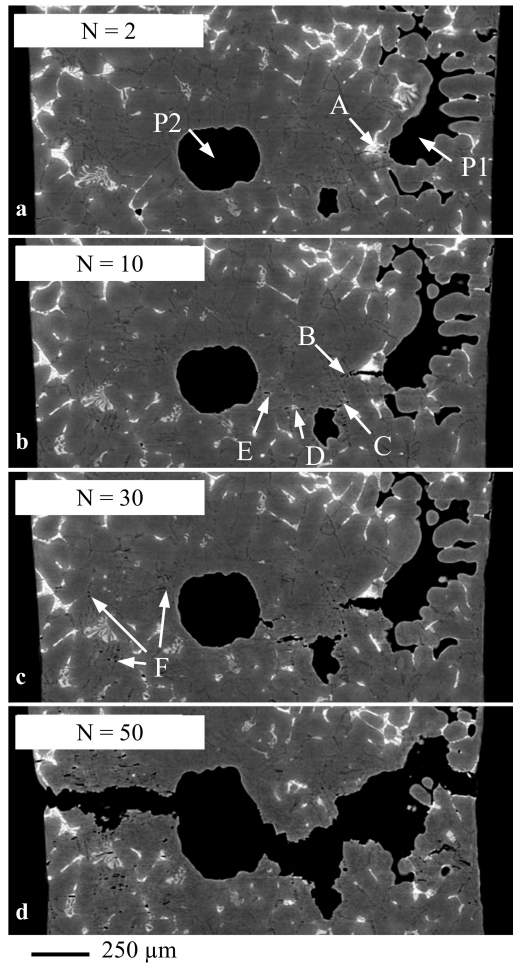


Figure 6: Tomographic slices made along a plane close to maximum damage and crack growth plane, for (a) 2 cycles, (b) 10 cycles, (c) 30 cycles, and (d) 50 cycles. The load direction is vertical and the labels on subfigures show pores (P1 and P2) or broken particles. θ -Al₂Cu: labels A and D, and Si particles: labels B,C,E and F.

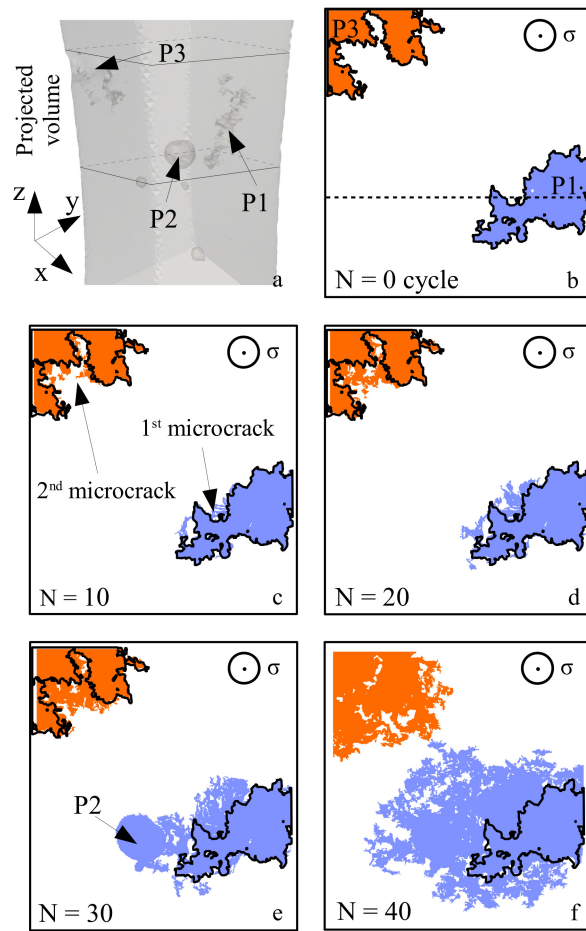


Figure 7: Damage projection on a plane orthogonal to the loading direction within the volume delimited by the continuous black lines of the subfigure (a). Dashed line in figure 7b indicates the position of the slices observed on figure 6.

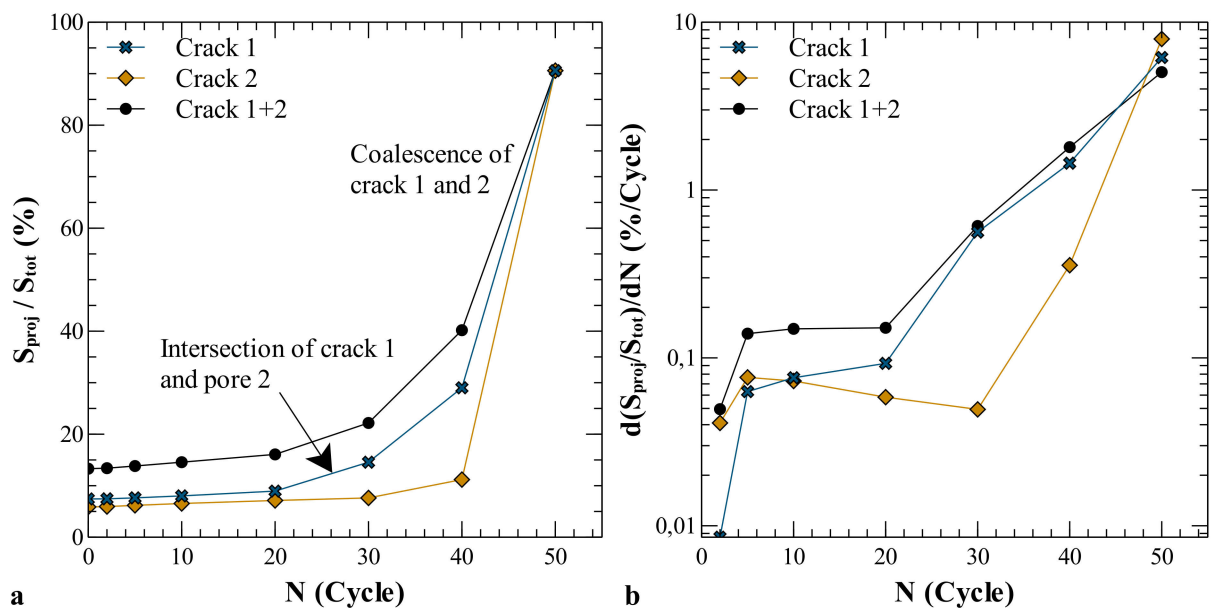


Figure 8: Evolution of the: (a) projected surfaces (S_{proj}) of cracks in percent of the total surface (S_{tot}) and (b) derived relative surface growth rates.

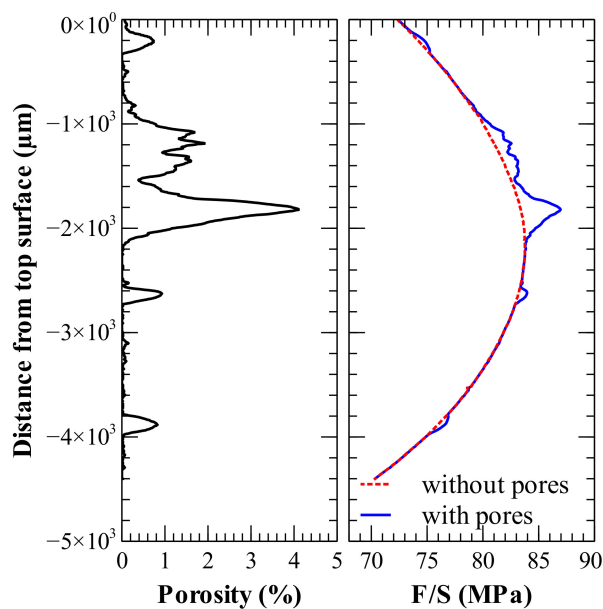


Figure 9: Slice by slice evolution (from the top of the observed volume) of the local pore volume fraction on the cross section area and the F/S ratios.

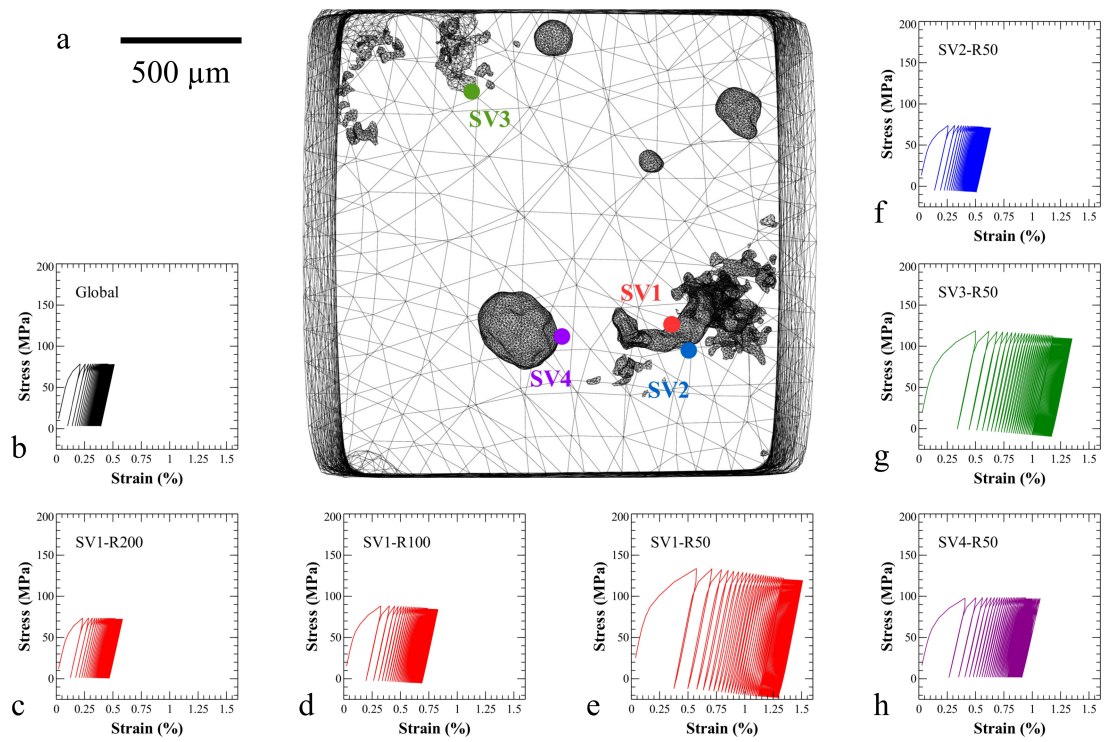


Figure 10: Top view of the specimen mesh (a). Points SV1, SV2, SV3 and SV4 correspond to the respective center of spherical subvolumes used for local analysis of the computed mechanical fields. Subfigures (b) to (h) show stress/strain cyclic curves for seven subvolumes using EVP simulations. See the text and table 3 and 4 for details.

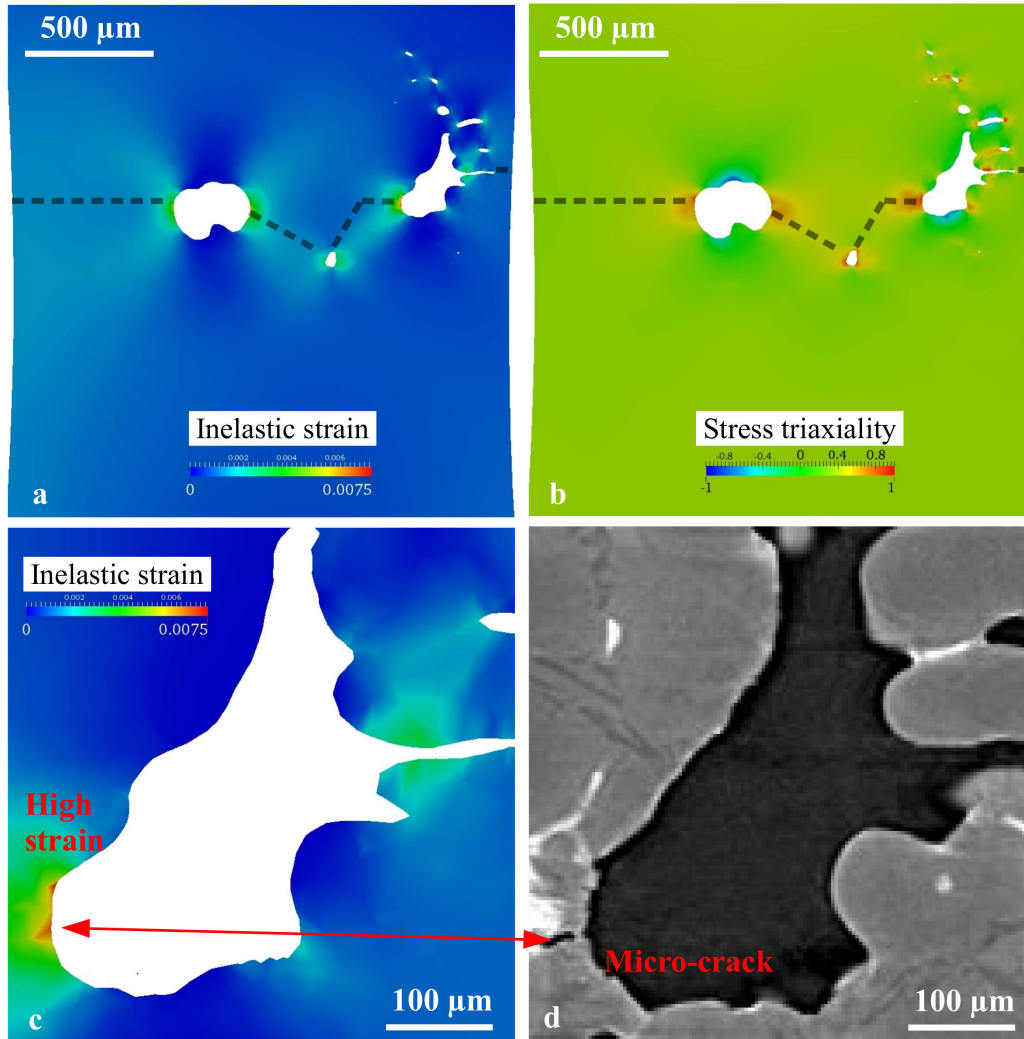


Figure 11: FE results after 3 cycles at maximum load on a cross section of the specimen corresponding to the plane of figure 6: (a) the inelastic strain and (b) the stress triaxiality. The values of the stress triaxiality shown are thresholded and bounded inside the $]-1;1[$ interval in order to facilitate the visualization. (c) Magnification of the inelastic strain around the shrinkage and (d) tomographic slice showing the first initiation site ($N=1$ cycle). The values of the stress triaxiality shown are thresholded and bounded inside the $]-1;1[$ interval in order to facilitate the visualization. The dashed lines on subfigures a and b represent the schematic final crack path.

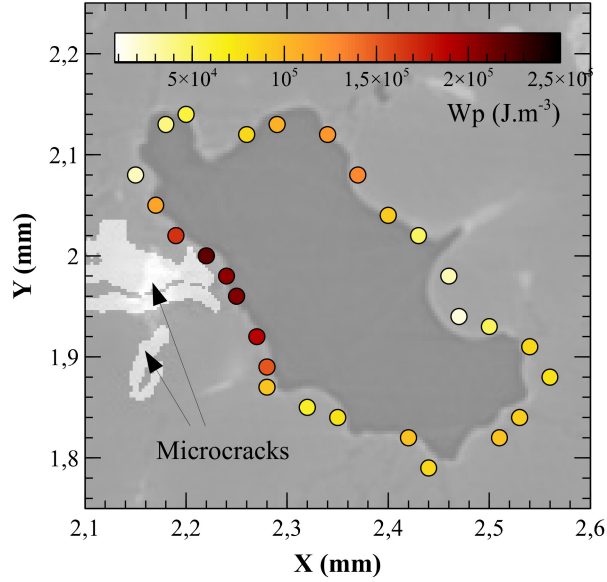


Figure 12: Computed inelastic strain energies around the shrinkage cavity on the critical plane identified on figure 9 orthogonal to the loading direction. Spherical subvolumes of $50\ \mu\text{m}$ radii centered on the defect surface were used for post-treatment analysis. Corresponding tomographic slice at initial state and the projection of the first microcracks at $N=5$ cycles appear respectively in background and foreground.

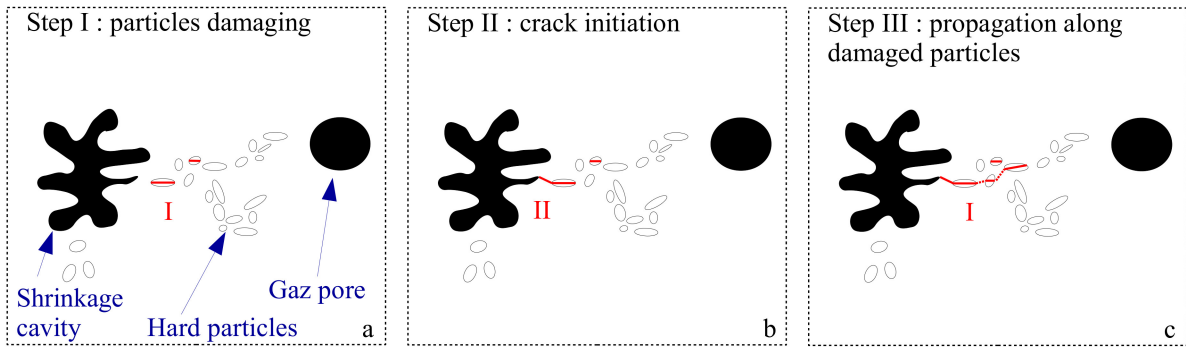


Figure 13: Schematic illustration of crack initiation and propagation mechanisms, a) damaging of hard particles during first cycles (step I), b) crack initiation by linking of pore and damaged area (step II), and c) crack growth by repetition of step I & II in front of the crack tip (step III).